VNU Journal of Science: Mathematics – Physics, Vol. 39, No. 1 (2023) 95-111

VNU Journal of Science: Mathematics - Physics

Journal homepage: https://js.vnu.edu.vn/MaP

Original Article

Determination of the Optimum Values of the Natural Frequency of the Nanocomposite Multilayer Organic Solar Cell by using Basic Differential Evolution Optimization Algorithms

Vu Minh Anh*

VNU University of Engineering and Technology, 144 Xuan Thuy, Cau Giay, Hanoi, Vietnam

Received 08 September 2022
Revised 02 October 2022; Accepted 24 October 2022

Abstract: By the analytical approach, the equation of natural frequency of nanocomposite multilayer organic solar cell (NMOSC) is analyzed in this work. The NMOSC is composed of 6 layers: Al, LiF, P3HT: PCBM, PEDOT: PSS, ITO and Glass. By using the classical plate theory, the Hooke's Law, the geometrical compatibility equation and the nonlinear equilibrium equations are proposed. These equations combined with the Galerkin method in order to investigate the effect of elastic foundations, geometrical parameters and initial imperfection on the natural frequency. Besides, in order to determine the maximum natural frequency of NMOSC, basic differential evolution optimization algorithm (DE) was used with five variables: elastic foundations include Winkeler foudation and Pasternak foudation, temperature, width and length. In the numerical results, the influence of length to width ratio, imperfection, elastic foundations and temperature increment were evaluated in detail. The optimal results from DE algorithm are shown and compared.

Keywords: Nonlinear dynamic, Organic solar cell, geometric optimization, DE.

1. Introduction

Solar energy is an electrical energy source that is manufactured by converting sunlight to electric power by using solar cell component based on the photoelectric effect. Nowadays, solar cell is considered a green energy source, a renewable energy source that contributes positively to sustaining

* Corresponding author.
E-mail address: vuminhanhhp@gmail.com

https//doi.org/10.25073/2588-1124/vnumap.4773

life on the earth. Besides, solar energy is widely applied in life because of advantages such as: high usage time, great flexibility, lightweight, cost savings. Jamali et al., [1] considered the impact of strain in the interface of different layers of solar cells has been investigated with density functional theory (DFT) and finite-difference time-domain (FDTD) techniques. The authors have simulated complex issue of strain and relaxation of atomic layers by using a new, effective and simple method and using a precise meshing technique. The lattice strain is included in both simple and gradient patterns in the theoretical simulations. Roca et al., [2] researched simulation of organic solar cells's power conversion efficiency. Krisha et al., [3] used P3HT:PCBM polymer as an active layer in the simulated organic solar cells (OSCs). The authors shown the results of the simulation of the power conversion efficiency of organic solar cells (OSCs), as well as the optimization of the thickness of active layer for better efficiency. Hattab et al., [4] investigated numerical simulation of a new heterostructure CIGS/GaSe solar cell system using SCAPS-1D software. By using the novel graphene platelets (GPL) reinforced functionally graded porous (GPLR-FGP) stiffeners in the struture of perovskite solar cell (PSC), Bo et al., [5] presented the nonlinear dynamic characteristics of the PSC with GPLR- FGP stiffeners under blast load using the von-Karma geometric nonlinearity and the first-order shear deformation theory, the governing motion equations are derived by utilizing Airy's stress function and the Galerkin method. The aim of the study of Kang et al., [6] is the evaluation of the working efficiency of fully vacuum-free and solution-processed large-area organic solar cells (OSCs) were fabricated using a poly(3,4-ethylenedioxythiophene)-poly(styrenesulfonate) (PEDOT:PSS) polymer top electrode. Wang et al., [7] indicated that theoretical simulation and kinds of experimental results confirm that BETAB nanocrystals can effectively reduce the defect density of perovskite films. Duc et al., [8] used the classical plate theory, geometrical nonlinearity in Von Karman – Donnell sense, the Galerkin method and fourth – order Runge – Kutta method to investigate the effect of geometrical parameters, the thickness of layers, imperfections, and mechanical loads on the nonlinear dynamic response and nonlinear vibration of nanocompsite organic solar cell. Zhu et al., [9] deal with p-type tetrathiafulvalene derivative as the interface modification layer in non-fullerene organic solar cells with high performance. Caldiran et al., [10] presented the changing the device geometry and the photophysical properties of the active layer in organic solar cells (OSCs) is an effective way to change the power conversion efficiency (PCE) by using the PEDOT:PSS layer was coated on chemically cleaned ITO coated glass substrates and the P3HT:PCBM blend as an active layer was coated on top of PEDOT:PSS in the glove box. Kadam et al., [11] studied compositional dynamics of the electron transport layer (ZnO:PEIE) in P3HT:$PC_{61}BM$ organic solar cells. Kim et al., [12] elucidated the potential of MOF (metal- organic frameworks)-integrated DSSCs (Solid-state fiber dye-sensitized solar cells) in the development of solar cell devices with efficiency comparable to or better than that of conventional solar cells. Li et al., [13] proposed Intrinsically inert hyperbranched interlayer for enhanced stability of organic solar cells. Liu et al., [14] provided an overview about the research progress of flexible OSCs (F-OSCs), from the aspect of materials (including flexible electrodes, interfacial layers and photoactive layers), large-area fabrication techniques and potential applications. These advancements enable F-OSCs to achieve PCEs over 15% with high stability, and we will also discuss the problems in F-OSCs. Quyen and Duc [15] used classical theory to investigate the effect of geometrical parameters, elastic foundation, viscous damping on the natural frequency, relationship deflection – time of nanocomposite multilayer solar panel.

Due to the great properties such as high thermal conductivity, high electrical conductivity, high elasticity and flexibility, high hardness and thinnest material in the world, graphene material promises to become a material that is applied in many fields such as microchips, transistors in the field of electronics, batteries in the automotive sector or solar energy. Therefore, graphene materials are attracting the attention of scientists around the world. Shen et al., [16] foused on nonlinear vibration behavior of a simply supported, rectangular, single layer graphene sheet in thermal environments based

on thin plate theory with a von Kármán-type of kinematic nonlinearity. Yang et al., [17] used an energy based approach in order to investigate dynamic buckling analysis for a rotationally restrained functionally graded (FG) graphene nanoplatelets (GPLs) reinforced composite (FG-GPLRC) porous arch under a uniform step load. Nam and Lee [18] presented an intensive numerical study on the static and dynamic responses of smart functionally graded microplates with graphene platelets (GPLs) reinforcement under concur- rently mechanical and electrical loads by using refined plate theory (RPT), modified couple stress theory (MCST) and NURBS-based isogeometric analysis (IGA). By using Halpin–Tsai's model, Lu et al., [19] predicted the effective Young's modulus of the axially moving graphene reinforced laminated composite plate in order to study the dynamic stability of an axially moving graphene reinforced laminated composite plate. Lu et al., [20] evaluated the role of the graphene platelets, weight fraction, microstructure effect, axial load as well as geometrical parameters on the free vibration and dynamic stability characteristics of functionally graded composite multilayer microtubes. based on the first-order shear deformation plate theory, von Karman nonlinear geometric relationship and Hamilton's principle, Mao et al., [21] proposed using graphene to enhance thermomechanical static and dynamic behaviors for functionally graded reinforced aluminium-based (GRA) composite plate. Kumar et al., [22] proposed a graphene based metasurface exhibiting dynamic slow light behavior via electromagnetically induced transparency (EIT) effect in the terahertz regime. Gong et al., [23] surveyed the influnece of a monolayer graphene metasurface which is composed of a graphene cross and four graphene side- strips on top of a metal film sandwiched by a dielectric spacer on a dynamically tunable triple-band terahertz perfect absorber. Kim et al., [24] presented the role of oxygen defects engineering via passivation of the Al_2O_3 interfacial layer for the direct growth of a graphene-silicon Schottky junction solar cell. Jang et al., [25] employed graphene quantum dots (GQDs) as an interfacial layer for better band alignment at the graphene (GR) transparent conductive electrode (TCE)/PSi interface. Yusuf et al., [26] presented method to enhance the performance of the MoO3 was made by doping graphene oxides (GO) using the spray pyrolysis technique. The reseach of Lu et al., [27] indecated that the introduction of graphene quantum dots effectively improved the morphology of the SnO_2 film, reduced the roughness of the surface, and increased the ohmic contact between the SnO_2 and perovskite layer. Gong et al., [28] discussed the roles of graphene and its derivatives in perovskite solar cells: A review. Gao et al., [29] introduced a high performance perovskite solar cell based on graphene-$CuInS_2$ QDs composite was fabricated. And an improved power conversion efficiency of 17.1% is achieved.

Optimizing for structures, the objective function is usually maximum natural frequency or critical buckling load with input variables such as thickness, height, width and so on. The optimization problem is interesting to scientists around the world such as Li et al., [30] focused on lightweight optimum design of head pressure shell of an autonomous underwater vehicle (AUV) with reliability requirements with the effect of the randomness of geometry sizes, material properties and loads by using genetic al- gorithm (GA) based on back propagation (BP) neural network surrogate model, which is optimized by particle swarm optimization (PSO) for improving accuracy. In order to investigate the effi- ciency of Non fullerene acceptor (NFA) based bulk heterojunction organic solar cell (NFA BHJ- OSC) including numerous electron transport layers (ETLs) such as TiO_2, SnO_2, and C60 and hole transport layers (HTLs) such as CuI, CuSCN, and Cu_2OA; Katariya et al., [31] simulated solar cell capacitance simulator (SCAPS). An optimization design strategy was developed by Nyangi and Ye [32] based on the performance requirements and expressed as a constrained multi-objective optimization design problem, where by the displacement response ratios of isolation layers were adopted as the constraints, and the acceleration response ratio of the super-structure was selected as the objective function. A new superstructure of supercritical CO_2 cycle for waste heat recovery based on the concept of splitting, which could optimization system structure and design parameters simulta- neously are studied by Yang et al. [33]. Elephant clan optimization: A nature-inspired metaheuristic algorithm for the optimal design of

structures by using a more powerful algorithm which called elephant clan optimization (ECO) are presented by Jafari et al., [34] to solve structural optimization problems. Hati and Panda [35] carried out the optimization design problem with two objectives considered in the present investigation are: minimization of the mass of attached sections and maximization of the extra residual life of structure due to mass attachment. The design variables of the optimization design problem are taken as the cross-sectional area of attached sections in the structure. Balaghi et al., [36] evaluated the dynamic history response by using a fuzzy version of BMD, which is developed as the premier method for prediction of peak response value of structures to be used within genetic algorithm (GA) optimization. Jafari et al., [37] used using a hybrid method based on particle swarm optimizer and cultural algorithm in order to proposed Optimal design of truss structures. Talatahari et al., [38] proposed using migration-based vibrating particles system to optimum design of steel building structures. An efficient eigensolution method for free vi- bration analysis of rotationally repetitive structures is developed for the optimal design of cyclic symmetric structures subject to frequency constraints in the study of Kaveh et al., [39]. In order to detemine the maximum value of natural frequency of plate with some variables as length, wigth, elastic foundations, Anh et al., [40] proposed using optimization algorithms (Bees Algorithm, Basic differential evolution algorithm, enhanced colliding bodies optimization algorithm, social group optimization algorithm). Liao et al., [41] indecated that optimization of solvent swelling for efficient organic solar cells via sequential deposition.

As seen from the literature review, this work proposes to use the DE in order to determine the maximum natural frequency of nanocomposite multilayer organic solar in the thermal environment based on the classical theory. By using Galerkin method, the governing equations are solved to indicate the effect of four variables: geometrical parameter, elastic foundations, thermal environment and imperfection on the natural frequency.

2. Problem Statement

Consider a rectangular NMOSC plate on elastic foundations which is composed by six layers: Al, LiF, P3HT:PCBM, PEDOT:PSS, ITO and Glass with length a, width b and total thickness h. The plate is referred to a Cartesian coordinate system x, y, z, where xy is the midplane of the plate and z is the thickness coordinator, $-h/2 \le z \le h/2$ (Fig. 1).

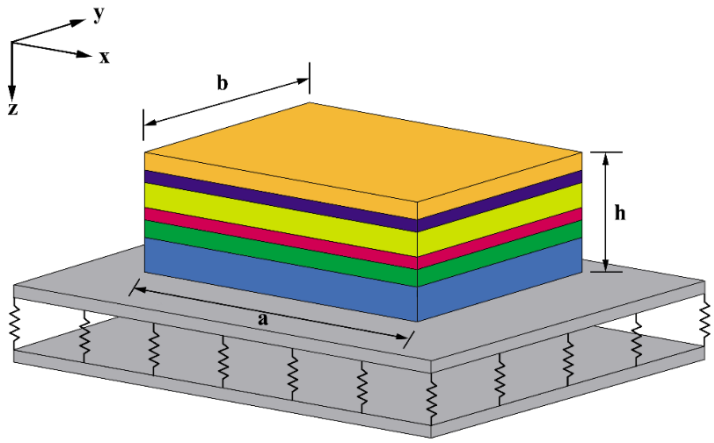

Figure 1. Geometry of the NMOSC plate on elastic foundations.

3. Theoretical Development

In this work, in order to investigate the nonlinear dynamic response of the NMOSC on elastic foundation in thermal environment, the classical plate theory is used [42, 43].

The strain field of the plate can be written as

$$\begin{pmatrix} \varepsilon_x \\ \varepsilon_y \\ \gamma_{xy} \end{pmatrix} = \begin{pmatrix} \varepsilon_{0x} \\ \varepsilon_{0y} \\ \gamma_{0xy} \end{pmatrix} + z \begin{pmatrix} \varepsilon_{1x} \\ \varepsilon_{1y} \\ \gamma_{1xy} \end{pmatrix} \text{ with } (\varepsilon_1) = \begin{pmatrix} \varepsilon_{1x} \\ \varepsilon_{1y} \\ \gamma_{1xy} \end{pmatrix} = \begin{pmatrix} -\dfrac{\partial^2 \mathrm{w}}{\partial x^2} \\ -\dfrac{\partial^2 \mathrm{w}}{\partial y^2} \\ -2\dfrac{\partial^2 \mathrm{w}}{\partial x \partial y} \end{pmatrix} \tag{1}$$

The strain - displacement relations for the NMOSC taking into account von Karman nonlinear terms is written as

$$(\varepsilon_0) = \begin{pmatrix} \varepsilon_{0x} \\ \varepsilon_{0y} \\ \gamma_{0xy} \end{pmatrix} = \begin{pmatrix} \dfrac{\partial u}{\partial x} + \dfrac{1}{2}\left(\dfrac{\partial \mathrm{w}}{\partial x}\right)^2 \\ \dfrac{\partial v}{\partial y} + \dfrac{1}{2}\left(\dfrac{\partial \mathrm{w}}{\partial y}\right)^2 \\ \dfrac{\partial u}{\partial y} + \dfrac{\partial v}{\partial x} + \dfrac{\partial \mathrm{w}}{\partial x}\dfrac{\partial \mathrm{w}}{\partial y} \end{pmatrix} \tag{2}$$

where u, v are the displacement components along the x, y directions, respectively.

The Hooke's Law shows the relationships between strain and stress for the NMOSC with *k*-th layer are written as

$$\begin{aligned} \left(\sigma_x, \sigma_y\right)_k &= \frac{E_k}{1-\nu_k^2}\left[\left(\varepsilon_x, \varepsilon_y\right) + \nu_k\left(\varepsilon_y, \varepsilon_x\right) - \left(1+\nu_k\right)\alpha_k \Delta T\right], \\ \left(\sigma_{xy}\right)_k &= \frac{E_k}{2(1+\nu_k)}\gamma_{xy}. \end{aligned} \tag{3}$$

in which E_k, ν_k are the Young's modulus and Poisson's ratio of the *k*-th layer

Based on the thickness and stress of each components, the equation force and moment for the NMOSC are shown as

$$\begin{aligned} (N_x, N_{,y}, N_{,xy}) &= \sum_{k=1}^{6} \int_{a_{k-1}}^{a_k} \left(\sigma_x, \sigma_y, \sigma_{xy}\right)_k dz, \\ (M_x, M_y, M_{xy}) &= \sum_{k=1}^{6} \int_{a_{k-1}}^{a_k} \left(\sigma_x, \sigma_y, \sigma_{xy}\right)_k z dz. \end{aligned} \tag{4}$$

Replacing Eqs. (1) and (2) into Eq. (3) then into Eq. (4) to obtain the detail relationship as

$$\begin{aligned} &\left(N_x, N_y\right) = \left(A_{10}, B_{10}\right)\varepsilon_{0x} + (A_{11}, B_{11})\varepsilon_{1x} + \left(B_{10}, A_{10}\right)\varepsilon_{0y} + (B_{11}, A_{11})\varepsilon_{1y} + C_{10}\Delta T \\ &N_{xy} = D_{10}\gamma_{0xy} + D_{11}\gamma_{1xy}, \\ &\left(M_x, M_y\right) = \left(A_{11}, B_{11}\right)\varepsilon_{0x} + (A_{12}, B_{12})\varepsilon_{1x} + \left(B_{11}, A_{11}\right)\varepsilon_{0y} + (B_{12}, A_{12})\varepsilon_{1y} + C_{11}\Delta T, \\ &M_{xy} = D_{11}\gamma_{0xy} + D_{12}\gamma_{1xy}. \end{aligned} \tag{5}$$

in which

$$A_{1i}=\sum_{k=1}^{6}\int_{a_{k-1}}^{a_k}\frac{E_k.z^i}{1-\nu_k^2}dz, B_{1i}=\sum_{k=1}^{6}\int_{a_{k-1}}^{a_k}\frac{E_k.\nu_k.z^i}{1-\nu_k^2}dz,$$

$$C_{1i}=-\sum_{k=1}^{6}\int_{a_{k-1}}^{a_k}\frac{E_k.\alpha_k.z^i}{1-\nu_k}dz,$$

$$D_{1i}=\frac{1}{2}\sum_{k=1}^{6}\int_{a_{k-1}}^{a_k}\frac{E_k.z^i}{1+\nu_k}dz=\frac{1}{2}\left(A_{1i}-B_{1i}\right).$$

The nonlinear dynamic response of the NMOSC with the effect of elastic foundations are shown in the nonlinear motion equations based on the classical plate theory as [43]

$$\frac{\partial N_x}{\partial x}+\frac{\partial N_{xy}}{\partial y}=\rho h\frac{\partial^2 u}{\partial t^2}+C_d\rho h\frac{\partial u}{\partial t},$$

$$\frac{\partial N_{xy}}{\partial x}+\frac{\partial N_y}{\partial y}=\rho h\frac{\partial^2 v}{\partial t^2}+C_d\rho h\frac{\partial v}{\partial t}, \tag{6}$$

$$\frac{\partial^2 M_x}{\partial x^2}+2\frac{\partial^2 M_{xy}}{\partial x\partial y}+\frac{\partial^2 M_y}{\partial y^2}+N_x\frac{\partial^2 w}{\partial x^2}+2N_{xy}\frac{\partial^2 w}{\partial x\partial y}+N_y\frac{\partial^2 w}{\partial y^2}$$

$$+q-k_w w+k_p\left(\frac{\partial^2 w}{\partial x^2}+\frac{\partial^2 w}{\partial y^2}\right)=\rho h\frac{\partial^2 w}{\partial t^2}+C_d\rho h\frac{\partial w}{\partial t}.$$

with C_{d} is the viscous damping coefficient, k_w, k_p are elastic foudations Winkler and Plasternak, respectively.

The stress function $f(x,y)$ is introduced as

$$N_x=f_{,yy}, N_y=f_{,xx}, N_{xy}=-f_{,xy}. \tag{7}$$

Replacing Eq. (7) into the three first equations of system Eq. (5), we have

$$\varepsilon_{0x}=E_1\left(A_{10}f_{,yy}-B_{10}f_{,xx}+E_2 w_{,x^2}+E_3 w_{,y^2}-E_4 C_{10}\Delta T\right),$$

$$\varepsilon_{0y}=E_1\left(A_{10}f_{,xx}-B_{10}f_{,yy}+E_2 w_{,y^2}+E_3 w_{,x^2}-E_4 C_{10}\Delta T\right), \tag{8}$$

$$\gamma_{0xy}=\frac{2D_{11}w_{,xy}-f_{,xy}}{D_{10}}.$$

with $E_1=\frac{1}{A_{10}^2-B_{10}^2}$; $E_2=A_{10}A_{11}-B_{10}B_{11}$; $E_3=A_{10}B_{11}-A_{11}B_{10}$; $E_4=A_{10}-B_{10}$.

The strains are related in the compatibility equation [42, 43]

$$\frac{\partial^2\varepsilon_{0x}}{\partial y^2}+\frac{\partial^2\varepsilon_{0y}}{\partial x^2}-\frac{\partial^2\gamma_{0xy}}{\partial x\partial y}=\left(\frac{\partial^2 \mathrm{w}}{\partial x\partial y}\right)^2-\frac{\partial^2 \mathrm{w}}{\partial x^2}\frac{\partial^2 \mathrm{w}}{\partial y^2}+2\frac{\partial^2 \mathrm{w}}{\partial x\partial y}\frac{\partial^2 \mathrm{w}^*}{\partial x\partial y}-\frac{\partial^2 \mathrm{w}}{\partial x^2}\frac{\partial^2 \mathrm{w}^*}{\partial y^2}-\frac{\partial^2 \mathrm{w}}{\partial y^2}\frac{\partial^2 \mathrm{w}^*}{\partial x^2}. \tag{9}$$

The third equation of system Eq. (6) is rewritten by using the Eq. (8) combined with Eq. (5)

$$\begin{aligned}
&\frac{\partial N_x}{\partial x}+\frac{\partial N_{xy}}{\partial y}=\rho h\frac{\partial^2 u}{\partial t^2}+C_d\rho h\frac{\partial u}{\partial t},\\
&\frac{\partial N_{xy}}{\partial x}+\frac{\partial N_y}{\partial y}=\rho h\frac{\partial^2 v}{\partial t^2}+C_d\rho h\frac{\partial v}{\partial t},\\
&T_1\phi^4 f+T_2\phi^4 w+\frac{\partial^2 f}{\partial y^2}\left(\frac{\partial^2 w}{\partial x^2}+\frac{\partial^2 w^*}{\partial x^2}\right)-2\frac{\partial^2 f}{\partial x\partial y}\left(\frac{\partial^2 w}{\partial x\partial y}+\frac{\partial^2 w^*}{\partial x\partial y}\right)\\
&+\frac{\partial^2 f}{\partial x^2}\left(\frac{\partial^2 w}{\partial y^2}+\frac{\partial^2 w^*}{\partial y^2}\right)+q-k_w w+k_p\left(\frac{\partial^2 w}{\partial x^2}+\frac{\partial^2 w}{\partial y^2}\right)\\
&=\rho h\frac{\partial^2 w}{\partial t^2}+C_d\rho h\frac{\partial w}{\partial t}.
\end{aligned} \tag{10}$$

where

$$T_1=E_1E_3, T_2=E_1\left(A_{11}E_2+B_{11}E_3\right)-A_{12},$$

$$\phi^4=\frac{\partial^4}{\partial x^4}+2\frac{\partial^4}{\partial x^2y^2}+\frac{\partial^4}{\partial y^4}.$$

By using Eqs. (9) and Eq. (8), the geometrical compatibility equation are written as

$$T_3\phi^4 f+T_4\phi^4 \mathrm{w}=\left(\frac{\partial^2 \mathrm{w}}{\partial x\partial y}\right)^2-\frac{\partial^2 \mathrm{w}}{\partial x^2}\frac{\partial^2 \mathrm{w}}{\partial y^2}+2\frac{\partial^2 \mathrm{w}}{\partial x\partial y}\frac{\partial^2 \mathrm{w}^*}{\partial x\partial y}-\frac{\partial^2 \mathrm{w}}{\partial x^2}\frac{\partial^2 \mathrm{w}^*}{\partial y^2}-\frac{\partial^2 \mathrm{w}}{\partial y^2}\frac{\partial^2 \mathrm{w}}{\partial x^2}. \tag{11}$$

In order to investigate the nonlinear dynamic response of imperfect NMOSC under the effect of elastic foundations in thermal environment based on the classical plate theory, the Eqs. (10) and (11) are used with two variables: the stress function f and the deflection w.

4. Nonlinear Dynanmic Response

Four edges of the plate are simply supported and immovable (IM). In this case, boundary conditions are

$$\begin{aligned}
&w=N_{xy}=M_x=0,\ N_x=N_x^0 \text{ at } x=0,\ a,\\
&w=N_{xy}=M_y=0,\ N_y=N_y^0 \text{ at } y=0,\ b.
\end{aligned} \tag{12}$$

where N_x^0, N_y^0 are fictitious compressive edge loads at immovable edges.

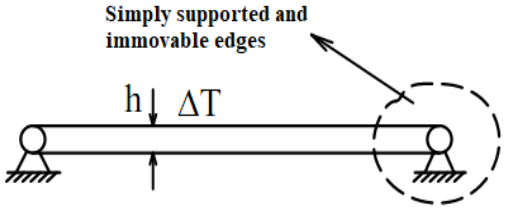

Figure 2. Description of the boundary conditions of the NMOSC.

In order to fulfill conditions (12), the deflection W and initial imperfection w^* are defined to be in cyclic form as [8]

$$w = W \sin \lambda_m x \sin \delta_n y, \tag{13}$$
$$w^* = \mu h \sin \lambda_m x \sin \delta_n y,$$

in which

$\alpha = \frac{m\pi}{a}, \beta = \frac{n\pi}{b}$

m, n are natural numbers of half waves in the x and y directions, respectively; $W(t)$ is the time dependent amplitude and μ is imperfection parameter of the NMOSC $(0 \le \mu \le 1)$.

Replacing Eq. (18) into the compatibility Eq, (16), the stress function f are determined as

$$f = C_1 \cos 2\lambda_m x + C_2 \cos 2\delta_n y + C_3 \sin \lambda_m x \sin \delta_n y + C_4 \cos 2\lambda_m x \cos 2\delta_n y + \frac{1}{2} N_{x0} y^2 + \frac{1}{2} N_{y0} x^2. \tag{14}$$

with

$$C_1 = \frac{W\delta_n^2 (W + 2\mu h)}{32 T_3 \lambda_m^2}, C_2 = \frac{W\lambda_m^2 (W + 2\mu h)}{32 T_3 \delta_n^2}, C_3 = -\frac{E_3 W}{A_{10}}, C_4 = 0. \tag{15}$$

Replacement of Eqs. (14) and (15) into Eq (10) then applying the Bubnov – Galerkin method leads to

$$P_1 W + P_2 q + P_3 (W + \mu h) + P_4 W (W + 2\mu h) + P_5 W (W + \mu h)$$
$$+ P_6 W (W + 2\mu h)(W + \mu h) = \rho h \frac{\partial^2 W}{\partial t^2} + C_d \rho h \frac{\partial W}{\partial t}. \tag{16}$$

in which

$$P_1 = \left(T_2 - \frac{T_1 E_3}{A_{10}} \right) \left(\lambda_m^2 + \delta_n^2 \right)^2 - k_w - k_p \left(\lambda_m^2 + \delta_n^2 \right), P_2 = \frac{16}{mn\pi^2},$$
$$P_3 = -\left(N_{x0} \lambda_m^2 + N_{y0} \delta_n^2 \right), P_4 = -\frac{16}{3} \frac{E_3 \delta_n^2 \lambda_m^2}{A_{10} mn\pi^2}, P_5 = -\frac{32}{9} \frac{E_3 \lambda_m \delta_n}{A_{10} ab}, P_6 = -\frac{1}{16 T_3} \left(\lambda_m^4 + \delta_n^4 \right).$$

Consider four edges of plate are assumed to be immovable and simply supported in the plane xy (i.e. $u = 0$ at $x = 0, a$ and $v = 0$ at $y = 0, b$) under the effect of temperature. The condition expressing the immovability on the edges as

$$\int_0^b \int_0^a \frac{\partial u}{\partial x} dx dy = 0, \int_0^a \int_0^b \frac{\partial v}{\partial x} dy dx = 0. \tag{17}$$

Eq. (25) denotes the relationship of $\frac{\partial u}{\partial x}, \frac{\partial v}{\partial y}$ dependent on two variables: the stress function f and the deflection W by using Eqs. (2) and (8) as

$$\begin{aligned}\frac{\partial u}{\partial x} &= E_1\left(A_{10} f_{,yy} - B_{10} f_{,xx} + E_2 w_{,x^2} + E_3 w_{,y^2} - E_4 C_{10}\Delta T\right) - \frac{w_{,x}^2}{2} - w_{,x} w_{,x}^*, \\ \frac{\partial v}{\partial y} &= E_1\left(A_{10} f_{,xx} - B_{10} f_{,yy} + E_2 w_{,y^2} + E_3 w_{,x^2} - E_4 C_{10}\Delta T\right) - \frac{w_{,y}^2}{2} - w_{,y} w_{,y}^*.\end{aligned} \tag{18}$$

In order to obtain the compressive edge loads, the Eqs. (14) and (15) are replaced into Eq. (18) then combine with Eq. (17) as

$$\begin{aligned}N_{x0} &= \alpha_1 \Delta T + \alpha_{12} W(W + 2\mu h) + \alpha_{13} W, \\ N_{y0} &= \alpha_1 \Delta T + \alpha_{22} W(W + 2\mu h) + \alpha_{23} W.\end{aligned} \tag{19}$$

with

$$\alpha_1 = (\mathrm{A}_{10} + \mathrm{B}_{10})\mathrm{E}_1\mathrm{E}_4\mathrm{C}_{10}, \alpha_{12} = \frac{\pi^2}{8}\left(\frac{A_{10}}{a^2} + \frac{B_{10}}{b^2}\right), \alpha_{22} = \frac{\pi^2}{8}\left(\frac{A_{10}}{b^2} + \frac{B_{10}}{a^2}\right),$$

$$\alpha_{13} = 4\left[\left(\frac{A_{10}}{a^2} + \frac{B_{10}}{b^2}\right)E_1E_2 + \left(\frac{A_{10}}{b^2} + \frac{B_{10}}{a^2}\right)E_1E_3 - \left(\frac{A_{10}^2}{b^2} - \frac{B_{10}^2}{b^2}\right)\frac{E_3}{A_{10}}E_1\right],$$

$$\alpha_{23} = 4\left[\left(\frac{A_{10}}{b^2} + \frac{B_{10}}{a^2}\right)E_1E_2 + \left(\frac{A_{10}}{a^2} + \frac{B_{10}}{b^2}\right)E_1E_3 - \left(\frac{A_{10}^2}{a^2} - \frac{B_{10}^2}{a^2}\right)\frac{E_3}{A_{10}}E_1\right].$$

Replacing Eq. (19) into Eqs. (16), we obtain

$$\begin{aligned}&K_1 W + K_2 Q\sin(\beta t) + K_3(W + \mu h) + K_4 W(W + 2\mu h) \\ &+ K_5 W(W + \mu h) + K_6 W(W + 2\mu h)(W + \mu h) = \rho h\frac{\partial^2 W}{\partial t^2} + C_d \rho h\frac{\partial W}{\partial t}.\end{aligned} \tag{20}$$

where

$$\begin{aligned}&K_1 = P_1,\ K_2 = P_2,\ K_3 = -\left[\alpha_1 \Delta T\left(\lambda_m^2 + \delta_n^2\right)\right], \\ &K_4 = P_4,\ K_5 = P_5 - \left(\lambda_m^2 \alpha_{13} + \delta_n^2 \alpha_{23}\right),\ K_6 = P_6 - \left(\lambda_m^2 \alpha_{12} + \delta_n^2 \alpha_{22}\right).\end{aligned}$$

The natural frequence of the NMOSC are shown in Eq. (21):

$$\omega_{mn} = \sqrt{-\frac{K_1 + K_3}{\rho h}}. \tag{21}$$

5. Optimal Design

5.1. Objective Function

From the formulas obtained above, we can see that parameters such as length a, width b, elastic foundation $k_{\mathrm{w},}\ k_p$ and the temperature increment ΔT directly affect the natural frequency of the NMOSC. Therefore, those five parameters are selected as five variables to determine the maximum natural frequency value with the objective function is defined by the Eq (21). The domain of five varibales are listed in Table 1.

Table 1. The domain of five variables.

Variable	Domain
$a(m)$	[0.1, 5]
$b(m)$	[0.1, 5]
$k_w(GPa/m)$	$[0,0.9]$
$k_p(GPa.m)$	$[0,0.09]$
$\Delta T(K)$	[0,1000]

5.2. Basic Differential Evolution Algorithm

The Basic Differential Evolution Algorithm (DE) was first introduced in the form of a technical report by two scientists Storn and Price [44] in 1995, is a word search algorithm random optimal solution. The DE algorithm is very efficient in handling problem of finding the extremes of non-differentiable, nonlinear functions and multi-objective function. DE algorithm flowchart includes initialization, mutation, crossover and selection steps. Details of the steps to implement the algorithm are shown in Fig. 3.

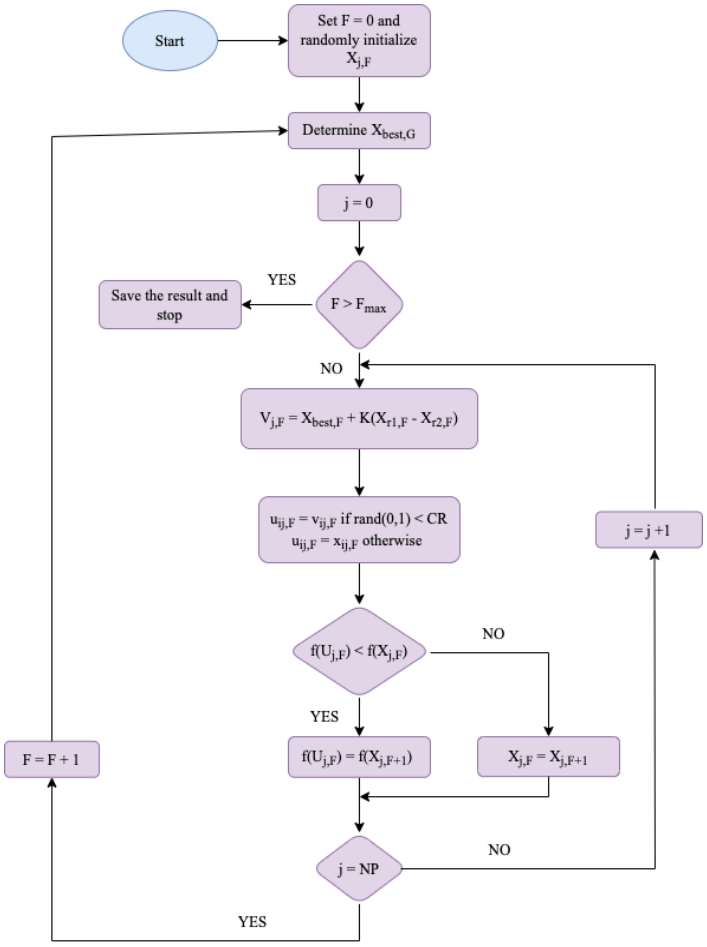

Figure 3. The flow chart for basic differential evolution algorithm (DE).

5.3. Particle Swarm Optimizaton Algorithm

In 1995, Kennedy and Eberhart [45] introduced the Particle swarm optimization (PSO) algorithm which was developed based on biological knowledge. The bio researchers indicated that when fish or birds move in a group, individuals can share the experience and information with all other members". For instance, when flying and reaching food, all birds of the group share information to have the best food source. PSO is simple one algorithm to search for optimal solution in the solution space with very few parameters.

6. Numerical Results and Discussion

The inital thickness and mechanical properties: Elastic modulus, possion ratio, density mas and thermal expression of six layers of NMOCS are shown in Table 2.

Table 2. The initial thickness and mechanical properties of six layers of NMOSC [3]

Material	$h\ (nm)$	$E\ (GPa)$	ν	$\rho\ (kg/m^3)$	$\alpha_{11}=\alpha_{22}\left(\times 10^{-6}K^{-1}\right)$
Al	100	70	0.35	2601	23
LiF	40	64.97	0.326	2635	37
P3HT:PCBM	170	6	0.23	1200	120
ITO	120	116	0.35	7120	6
PEDOT:PSS	50	2.3	0.4	1000	70
Glass	550000	69	0.23	2400	9

6.1. Validation

In order to validate the accuracy of used theory and calculation results, the natural frequency ω_{mn} of NMOSC are determined and compared with the results of Li et al. [46]. The compared results are shown in Table 3 by replacing $h_{LiF}=0$ to modeling in this paper became the modling in the paper of Li with $a/b=1,\ a/h=55,\ h=550440nm,\ \Delta T=0K$. We can see that the obtained results of natural frequencies of two paper has negligible error. Is is demonstrate that used theory and calculation results in this paper have high reliability.

Table 3. The compared results of natural frequency

(m,n)	Li et al., [45]	Present	Relative error (%)
(1, 1)	18847.75	19715	4.606
(1, 3)	94238.78	98576	4.603
(2, 2)	75391.02	78861	4.603
(2, 3)	122510.41	128150	4.604
(3, 3)	169629.80	177440	4.605

6.2. Dynamic Response

Table 4. The influence of a/b and mode (m,n) on the natural frequecies of NMOSC

a/b	(m,n)				
	(1,1)	(1,3)	(3,3)	(3,5)	(5,5)
1	803550	1798800	2416200	3328700	4046200
1.5	1024500	2626500	3085200	4632700	5181800
2	1271000	3474000	3835700	6026200	6468400
2.5	1531000	4334300	4632700	7480600	7852300

In this part, the results which are shown the influence of geometrical parameters, temperature increment, elastic foundation and mode (m,n) on the natural frequency of the NMOSC are analyzed in detail with condition is to keep the thickness value of six layers.

Table 4 shows the influence of a/b and mode (m,n) on the natural frequecies of NMOSC. It can be seen that when ratio a/b and mode (m,n) increases resutls in the natural frequencies also increase. The influence of a/h and k_w, k_p on the natural frequencies of NMOSC are illustrated in Table 5. It can see that the decreasing of natural frequencies when a/h ratio increase. Besides, the elastic foundations k_w and k_p have importance role on the improve the stiffness of the NMOSC. In details, the increasing of elastic foudation leads to the natural frequencies increase with same ratio a/h.

Table 5. The influence of a/h and k_w, k_p on the natural frequecies of NMOSC

a/h	$k_w\,(GPa/m)$, $k_p\,(GPa.m)$			
	0.1; 0.02	0.1; 0.04	0.2; 0.06	0.3; 0.08
20	1561000	2213984	2714000	3135400
35	889260	1263200	1549300	1790300
55	565430	803500	985700	1139100

Table 6 indicates that the increasing of temperature makes the decreasing of frequencies and with the same temperature variation, the increasing mode (m,n) leads to the increasing of natural frequencies of NMOSC.

Table 6. The influence of mode (m,n) and ΔT on the natural frequecies of NMOSC

(m,n)	ΔT				
	300	400	500	700	900
(1,1)	803550	802160	800780	798000	795210
(1,3)	1798800	1795700	1792600	1786400	1780200
(3,3)	2416200	2412100	2407900	2399600	2391200

6.3. Optimal Results

Table 7. The optimum values of the objective function with the value of five variables.

	DE	PSO
$\omega_L\,(1/s)$	367586.35	367586.35
$a\,(m)$	0.1	0.1
$b\,(m)$	0.1	0.1
$k_w\,(GPa/m)$	0.9	0.9
$k_p\,(GPa.m)$	0.09	0.09
$\Delta T\,(K)$	0	0
Time (s)	5.58	1.2

Table 7 gives the optimal values of the objective function and corresponding values of five variables when this paper uses DE algorithms. Besides, in order to validate the accuracy of DE algorithms, the obtained results of DE algorithms are compared with other results which are determined by using Particle swarm optimization (PSO). From Table 7, it can be seen that the results obtained from both algorithms are the similar but the time to complete 300 evaluations of the SPO algorithm is faster than that of the DE algorithm.

The process of finding the optimal value of the objective function is shown in Figure 4 with 300 times evaluation by using DE algorithm. After 30 times evaluation, the value of the natural frequency does not change. This also means that the maximum value of the objective function has been determined.

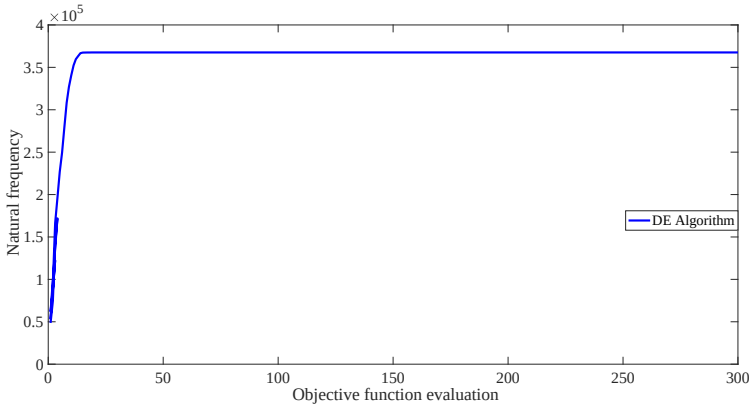

Figure 4. The convergence of natural frequencies by using DE algorithms.

By using the basic differential evolution algorithm – DE, Figure 5 presents the effect of the change of a/b ratio on the convergence of natural frequency, which is evaluated through the change value of the numbers of objective function evaluation. The increase of the maximum values of the natural frequency is directly proportional to the increasing of a/b ratio.

Table 8 describes the optimum values of objective function with the change value of a/b ratio and values of four variables in which basic differential evolution algorithm – DE is used. Clearly, the optimum values of objective function decrease when a/b ratio decreases.

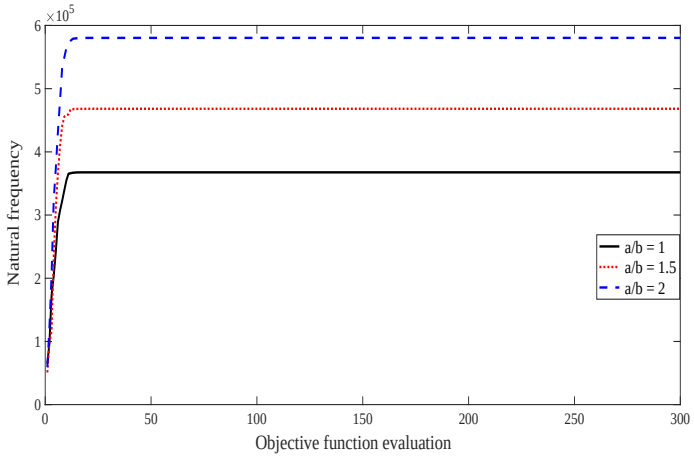

Figure 5. The convergence of natural frequency with the change value of a/b ratio.

Table 8. The optimum values of objective function with the change value of a/b ratio.

	$b=a$	$b=a/1.5$	$b=a/2$
$\omega_L(1/s)$	367586.35	468131.61	580336.08
$a(m)$	0.1	0.1	0.1
$k_w(GPa/m)$	0.9	0.9	0.9
$k_p(GPa.m)$	0.09	0.09	0.09
$\Delta T(K)$	0	0	0

7. Conclusion

By using the Galerkin method and classical plate theory, the narutral frequency equation is determined with the effect of a/b ratio, a/h ratio increment thermal, elastic foundations, imperfection and mode (m,n). The results using DE optimization algorithms which is used in order to research about the maximum value of natural frequency were evaluated in details. Outstanding obtained results of this study can be mentioned as follows.

i) The results of our work are compared with the works that were published in order to evaluate the accurracy of the used theory and method;

ii) The elastic foundations k_w and k_p have an important role in the improvement of the value of natural frequency of the NMOSC;

iii) The natural frequency of NMOSC is negatively affected by the temperature increment. It can be seen that the natural frequency increases when the temperature increment decreases;

iv) The mode (m,n) and a/b ratio makes the incresing natural frequency of the NMOSC. In contrast, the increasing of a/h ratio makes the decrease of natural frequency of the NMOSC;

v) The maximum values of objective function and five variables are determined by using DE. Besides, the influence of a/b ratio on the maximum values of objective function has also been considered.

Acknowledgments

This work has been supported by VNU University of Engineering and technology under project number CN21.21

References

[1] A. Jamali, M. Saffari, M. B. Tagani, H. R. Soleimani, A New and Simple Method for Simulation of Lattice Mismatch on the Optical Properties of Solar Cells: A Combination of DFT and FDTD Simulations, Solar Energy, Vol. 230, 2021, pp. 166-176, https://doi.org/10.1016/j.solener.2021.10.021.

[2] E. H. S. Rosa, E. L. Kowalski, L. F. R. B. Toledo, Simulation of Organic Solar Cells's Power Conversion Efficiency, Solar Energy, Vol. 221, 2021, pp. 483-487, https://doi.org/10.1016/j.solener.2021.04.016.

[3] B. G. Krishna, D. S. Ghosh, S. Tiwari, Progress in Ambient Air-processed Perovskite Solar Cells: Insights Into Processing Techniques and Stability Assessment, Solar Energy, Vol. 224, 2021, pp. 1369-1395, https://doi.org/10.1016/j.solener.2021.07.002.

[4] M. A. Hattab, L. Moudou, M. Khenfouch, O. Bajjou, Y. Chrafih, K. Rahmani, Numerical Simulation of A New Heterostructure CIGS/Gase Solar Cell System Using SCAPS-1D Software, Solar Energy, Vol. 227, 2021, pp. 13-22, https://doi.org/10.1016/j.solener.2021.08.084.

[5] L. Bo, Q. Li, Y. Tian, D. Wu, Y. Yu, X. Chen, W. Gao, Nonlinear Dynamic Investigation of the Perovskite Solar Cell with GPLR-FGP Stiffeners Under Blast Impact, International Journal of Mechanical Sciences, Vol. 213, 2022, pp. 106866, https://doi.org/10.1016/j.ijmecsci.2021.106866.

[6] M. H. Kang, T. Cheon, H. Kim, Fully Vacuum-free Large-area Organic Solar Cell Fabrication from Polymer Top Electrode, Solid-state Electronics, Vol. 186, 2021, pp. 108192, https://doi.org/10.1016/j.sse.2021.108192.

[7] X. Wang, Y. Qiu, L. Wang, T. Zhang, L. Zhu, T. Shan, Y. Wang, J. Jiang, L. Kong, H. Zhong, H. Yu, F. Liu, F. Gao, F. Wang, C. C. Chen, Organic Nanocrystals Induced Surface Passivation Towards High-Efficiency and Stable Perovskite Solar Cells, Nano Energy, Vol. 89, 2021, pp. 106445, https://doi.org/10.1016/j.nanoen.2021.106445.

[8] N. D. Duc, K. S. Eock, T. Q. Quan, D. D. Long, V. M. Anh, Nonlinear Dynamic Response and Vibration of Nanocomposite Multilayer Organic Solar Cell, Composite Structures, Vol. 184, 2018, pp. 1137-1144, https://doi.org/10.1016/j.compstruct.2017.10.064.

[9] Y. Zhu, L. Zhao, Z. Du, G. Chen, Y. Li, L. Wang, X. Xiao, P-type Tetrathiafulvalene Derivative as the Interface Modification Layer in Non-fullerene Organic Solar Cells with High Performance, Synthetic Metals, Vol. 282, 2021, pp. 116946, https://doi.org/10.1016/j.synthmet.2021.116946.

[10] Z. Çaldıran, Ü. Erkem, A. Baltakesmez, M. Biber, Effects of the PENTACENE as Doping Material on the Power Conversion Efficiency of P3HT:PCBM Based Ternary Organic Solar Cells, Physica B, Vol. 607, 2021, pp. 412859, https://doi.org/10.1016/j.physb.2021.412859.

[11] K. D. Kadam, H. Kim, S. Rehman, H. Patil, J. Aziz, T. D. Dongale, M. F. Khan, D. Kim, Compositional Dynamics of the Electron Transport Layer (ZnO:PEIE) in P3HT:PC_{61}BM Organic Solar Cells, Materials Science in Semiconductor Processing, Vol. 136, 2021, pp. 106118, https://doi.org/10.1016/j.mssp.2021.106118.

[12] J. H. Kim, H. W. Park, S. Koo, D. Lee, E. Cho, Y. Kim, M. Shin, J. W. Choi, H. J. Lee, M. Song, High Efficiency and Stable Solid-State Fiber Dye-sensitized Solar Cells Obtained Using TiO_2 Photoanodes Enhanced with Metal Organic Frameworks, Journal of Energy Chemistry, Vol. 67, 2022, pp. 458-466, https://doi.org/ 10.1016/j.jechem.2021.10.034.

[13] Y. Li, T. Li, J. Wang, X. Zhan, Y. Lin, Intrinsically Inert Hyperbranched Interlayer for Enhanced Stability of Organic Solar Cells, Science Bulletin, Vol. 26, 2022, pp. 171-177, https://doi.org/10.1016/j.scib.2021.09.013.

[14] C. Liu, C. Xiao, C. Xie, W. Li, Flexible Organic Solar Cells: Materials, Large-area Fabrication Techniques and Potential Applications, Nano Energy, Vol. 89, 2021, pp. 106399, https://doi.org/10.1016/j.nanoen.2021.106399.

[15] N. V. Quyen, N. D. Duc, Vibration and Nonlinear Dynamic Response of Nanocomposite Multi-layer Solar Panel Resting on Elastic Foundations, Thin – Walled Structures, Vol. 177, 2022, pp. 109412, https://doi.org/10.1016/j.tws.2022.109412.

[16] L. Shen, H. S. Shen, C. L. Zhang, Nonlocal Plate Model for Nonlinear Vibration of Single Layer Graphene Sheets in Thermal Environments, Computational Materials Science, Vol. 48, 2010, pp. 680-685, https://doi.org/10.1016/j.commatsci.2010.03.006.

[17] Z. Yang, D. Wu, J. Yang, S. Lai, J. Lv, A. Liu, J. Fu, Dynamic Buckling of Rotationally Restrained FG Porous Arches Reinforced with Graphene Nanoplatelets under a Uniform Step Load, Thin-walled Structures, Vol. 166, 2021, pp. 108103, https://doi.org/10.1016/j.tws.2021.108103.
[18] N. V. Nam, J. Lee, On the Static and Dynamic Responses of Smart Piezoelectric Functionally Graded Graphene Platelet-Reinforced Microplates, International Journal of Mechanical Sciences, Vol. 197, 2021, pp. 106310, https://doi.org/10.1016/j.ijmecsci.2021.106310.
[19] S. F. Lu, N. Xue, W. Zhang, X. J. Song, W. S. Ma, Dynamic Stability of Axially Moving Graphene Reinforced Laminated Composite Plate Under Constant and Varied Velocities, Thin-walled Structures, Vol. 167, 2021, pp. 108176, https://doi.org/10.1016/j.tws.2021.108176.
[20] L. Lu, S. Wang, M. Li, X. Guo, Free Vibration and Dynamic Stability of Functionally Graded Composite Microtubes Reinforced with Graphene Platelets, Composite Structures, Vol. 272, 2021, pp. 114231, https://doi.org/10.1016/j.compstruct.2021.114231.
[21] D. Kumar, K. M. Devi, R. Kumar, D. R. Chowdhury, Dynamically Tunable Slow Light Characteristics in Graphene Based Terahertz Metasurfaces, Optics Communications, Vol. 491, 2021, pp. 126949, https://doi.org/10.1016/j.optcom.2021.126949.
[22] J. J. Mao, W. Zhang, H. M. Lu, Static and Dynamic Analyses of Graphene-reinforced Aluminium-based Composite Plate in Thermal Environment, Aerospace Science and Technology, Vol. 107, 2020, pp. 106354, https://doi.org/10.1016/j.ast.2020.106354.
[23] J. Gong, X. Shi, Y. Lu, F. Hu, R. Zong, G. Li, Dynamically Tunable Triple-band Terahertz Perfect Absorber Based on Graphene Metasurface, Superlattices and Microstructures, Vol. 150, 2020, pp. 106797, https://doi.org/10.1016/j.spmi.2020.106797.
[24] M. Kim, M. A. Rehman, K. M. Kang, Y. Wang, S. Park, H. S. Lee, S. B. Roy, S. H. Chun, C. A. Singh, S. C. Jun, H. Park, The Role of Oxygen Defects Engineering Via Passivation of the Al_2O_3 Interfacial Layer for the Direct Growth of A Graphene-silicon Schottky Junction Solar Cell, Applied Materials Today, Vol. 26, 2022, pp. 101267, https://doi.org/10.1016/j.apmt.2021.101267.
[25] C. W. Jang, D. H. Shin, S. H. Choi, Porous Silicon Solar Cells with 13.66% Efficiency Achieved by Employing Graphene-quantum-dots Interfacial Layer, Doped-graphene Electrode, and Bathocuproine Back-Surface Passivation Layer, Journal of Alloys and Compounds, Vol. 877, 2021, pp. 160311, https://doi.org/10.1016/j.jallcom.2021.160311.
[26] B. Yusuf, M. R. Hashim, M. M. Halim, Efficiency Improvement of Molybdenum Oxide Doped with Graphene Oxide Thin Films Solar Cells Processed by Spray Pyrolysis Technique, Physica B, Vol. 625, 2022, pp. 413532, https://doi.org/10.1016/j.physb.2021.413532.
[27] C. Lu, W. Zhang, Z. Jiang, Y. Zhang, C. Ni, Graphene Quantum Dots Doping SnO_2 for Improving Carrier Transport of Perovskite Solar Cells, Ceramics International, Vol. 47, 2021, pp. 29712-29721, https://doi.org/10.1016/j.ceramint.2021.07.143.
[28] K. Gong, J. Hu, N. Cui, Y. Xue, L. Li, G. Long, S. Lin, The Roles of Graphene and Its Derivatives in Perovskite Solar Cells: A Review, Materials and Design, Vol. 211, 2021, pp. 110170, https://doi.org/10.1016/j.matdes.2021.110170.
[29] F. Gao, K. Liu, R. Cheng, Y. Zhang, Efficiency Enhancement of Perovskite Solar Cells Based on Graphene-$Cuins_2$ Quantum Dots Composite: The Roles for Fast Electron Injection and Light Harvests, Applied Surface Science, Vol. 528, 2020, pp. 146560, https://doi.org/10.1016/j.apsusc.2020.146560.
[30] N. Li, D. Q. Zhang, H. T. Liu, T. J. Li, Optimal Design and Strength Reliability Analysis of Pressure Shell with Grid Sandwich Structure, Ocean Engineering, Vol. 223, 2021, pp. 108657, https://doi.org/10.1016/j.oceaneng.2021.108657.
[31] A. Katariya, B. Mahapatra, P. K. Patel, J. Rani, Optimization of ETM and HTM Layer on NFA Based BHJ-organic Solar Cell for High Efficiency Performance, Optik, Vol. 245, 2021, pp. 167717, https://doi.org/10.1016/j.ijleo.2021.167717.
[32] P. Nyangi, K. Ye, Optimal Design of Dual Isolated Structure with Supplemental Tuned Inerter Damper Based on Performance Requirements, Soil Dynamics and Earthquake Engineering, Vol. 149, 2021, pp. 106830, https://doi.org/10.1016/j.soildyn.2021.106830.
[33] C. Yang, Y. Deng, N. Zhang, X. Zhang, G. He, J. Bao, Optimal Structure Design of Supercritical CO_2 Power Cycle for Gas Turbine Waste Heat Recovery: A Superstructure Method, Applied Thermal Engineering, Vol. 198, 2021, pp. 117515, https://doi.org/10.1016/j.applthermaleng.2021.117515.

[34] M. Jafari, E. Salajegheh, J. Salajegheh, Elephant clan optimization: A Nature-inspired Metaheuristic Algorithm for the Optimal Design of Structures, Applied Soft Computing, Vol. 113, 2021, pp. 107892, https://doi.org/10.1016/j.asoc.2021.107892.
[35] S. Hati, S. K. Panda, Game Theory Approach for Optimum Design of An Aged Structure with Multiple Objectives, Structures, Vol. 31, 2021, pp. 205-215, https://doi.org/10.1016/j.istruc.2021.01.097.
[36] S. Balaghi, S. S. Naseralavi, E. Khojastehfa, Optimal Design of Structures Under Earthquake Loads Using Basic Modal Displacements Method Enhanced by Fuzzy C-means Clustering, Structures, Vol. 32, 2021, pp. 778-791, https://doi.org/10.1016/j.istruc.2021.03.001.
[37] M. Jafari, E. Salajegheh, J. Salajegheh, Optimal Design of Truss Structures Using A Hybrid Method Based on Particle Swarm Optimizer and Cultural Algorithm, Structures, Vol. 32, 2021, pp. 391-405, https://doi.org/10.1016/j.istruc.2021.03.017.
[38] S. Talatahari, S. Jalili, M. Azizi, Optimum Design of Steel Building Structures Using Migration-based Vibrating Particles System, Structures, Vol. 33, 2021, pp. 1394-1413, https://doi.org/10.1016/j.istruc.2021.05.028.
[39] A. Kaveh, K. B. Hamedani, A. Joudaki, M. Kamalinejad, Optimal Analysis for Optimal Design of Cyclic Symmetric Structures Subject to Frequency Constraints, Structures, Vol. 33, 2021, pp. 3122-3136, https://doi.org/10.1016/j.istruc.2021.06.054.
[40] V. M. Anh, T. Q. Quan, P. Chan, Nonlinear Vibration and Geometric Optimization of Nanocomposite Multilayer Organic Solar Cell Under Wind Loading, Thin–walled Structures, Vol. 158, 2021, pp. 107199, https://doi.org/10.1016/j.tws.2020.107199.
[41] Q. Liao, B. Li, H. Sun, C. W. Koh, X. Zhang, B. Liu, H. Y. Woo, X. Guo, Optimization of Solvent Swelling for Efficient Organic Solar Cells Via Sequential Deposition, Materials Reports: Energy, Vol. 1, 2021, pp. 100063, https://doi.org/10.1016/j.matre.2021.100063.
[42] D. D. Brush, B. O. Almrothm, Buckling of Bars, Plates And Shells, McGraw-Hill Companies, 1975.
[43] J. N. Reddy, Mechanics of Laminated Composite Plates and Shells: Theory and Analysis, Boca Raton: CRC Press, 2004.
[44] R. Storn, K. Price, Differential Evolution - A Simple and Efficient Adaptive Scheme for Global Optimization Over Continuous Spaces, Journal of Global Opmization, Vol. 23, 1995.
[45] J. Kennedy, R. C. Eberhart, Particle Swarm Optimization, Proceedings of ICNN'95 - International Conference on Neural Networks,Vol. 4, 1995, pp. 1942-1948, https://doi.org/10.1109/ICNN.1995.488968.
[46] Q. Li, D. Wu, W. Gao, T. L. Francis, Z. Liu, J. Cheng, Static Bending and Free Vibration of Organic Solar Cell Resting on Winkler-pasternak Elastic Foundation Through The Modified Strain Gradient Theory, European Journal of Mechanics - A/Solids, Vol. 78, 2019, pp. 103852, https://doi.org/10.1016/j.euromechsol.2019.103852.